ISSN (Print) 1226-1750
ISSN (Online) 2233-6656
Journal of Magnetics 24(3), 371-378 (2019) https://doi.org/10.4283/JMAG.2019.24.3.371

Structural and Magnetic Properties of Gd-Ni-co-doped $BiFeO_3$ Nanoparticles

Sandeep Kumar Singh Patel[a], Jae-Hyeok Lee, Min-Kwan Kim, and Sang-Koog Kim*

National Creative Research Initiative Center for Spin Dynamics and Spin-Wave Devices, Nanospinics Laboratory, Research Institute of Advanced Materials, Department of Materials Science and Engineering, Seoul National University, Seoul 151-744, South Korea
[a]Current address: Department of Chemistry, S.R.P.S. College (B.R.A. Bihar University, Muzaffarpur) Jaintpur-843123, India

(Received 27 August 2019, Received in final form 24 September 2019, Accepted 25 September 2019)

Single-phase $(GdNi)_x(BiFe)_{1-x}O_3$ (x = 0, 0.025, and 0.05) nanoparticles of 30-40 nm particle size on average were fabricated using a sol-gel method. Transmission electron microscopy, X-ray diffraction as well as Raman spectral measurements and analyses revealed that the $(GdNi)_x(BiFe)_{1-x}O_3$ nanoparticles undergo a structural transformation from the rhombohedral *R3c* structure (for x = 0 and 0.025) to the triclinic *P1* (for x = 0.05). X-ray photoemission spectroscopy served to confirm that co-doping of Gd^{3+} and Ni^{2+} ions decreases oxygen-vacancy concentration, reflecting less Fe^{2+} content in the co-doped samples compared with pure $BiFeO_3$. Magnetization hysteresis loops showed that the magnetization value for x = 0.05 at 50 kOe increases significantly to M = 5.32 emu/g at 300 K and to 14.47 emu/g at 5 K, representing 760 and 690 % enhancements relative to those for x = 0. Fitting of the Curie-Weiss law to the observed magnetization-versus-temperature curves indicated the presence of weak ferromagnetic coupling in the samples. We also noted the exchange bias effect in the nano-size particles, possibly originating from exchange coupling between surface spins of an uncompensated ferromagnetic nature and core spins of an antiferromagnetic nature. We ascribed these significant improvements in the Gd-Ni-co-doped $BiFeO_3$ nanoparticles' magnetic properties to the rhombohedral *R3c* to triclinic *P1* structural transformation, due to the samples' particle size being smaller than the modulation length of the canted antiferromagnetic ordering of the Fe^{3+} spins. These enhanced magnetic properties, notably, might prove useful for a variety of spintronic applications.

Keywords : Gd/Ni co-doped BFO nanoparticles, Phase transformation, Dzyaloshinskii–Moriya interaction, Exchange-bias effect

1. Introduction

Over the past two decades, multiferroic materials have attracted great attention owing to their potential applications for robust spintronic and data-storage devices [1-3]. In this respect, $BiFeO_3$ is a well-known multiferroic material having both ferroelectric (Curie temperature $T_C \approx$ 1103 K) and G-type antiferromagnetic (Neel temperature $T_N \approx$ 643 K) properties above room temperature [4, 5]. Pure $BiFeO_3$ material has a typically distorted rhombohedral perovskite structure with an *R3c* space group at room temperature [6]. However, $BiFeO_3$'s practical application is limited by its low magnetic moment and weak magneto-dielectric coupling, both of which are due to the modulation of canted anti-ferromagnetic ordering of Fe^{3+} spins or spirally modulated spin configurations of approximately 62 nm wavelength [7]. One of the most effective means of suppressing such spiral magnetic ordering and enhancing BFO's net magnetization value is to reduce the dimensions of $BiFeO_3$ below the wavelength (62 nm) of the spirally modulated spin configuration. Another solution is to replace BFO's Bi^{3+} and Fe^{3+} ions with others of comparable size and with higher Bohr magnetic moment [8-19]. In order to tackle such issues, structural phase transformations of BFO have been achieved by substitution of rare-earth ions such as Nd [8, 11], La [10], Pr [12], Gd [15], Ho [9, 17, 18], and Dy [19], or of transition metal ions such as Ti [16], Mn [14, 15], and Co [13], or alternatively, by co-doping of La–Mn [20], Ca–Mn [21], La–Co [22] and (La, Pr)–Co [23]. To our best knowledge, there are as yet no studies on co-doping of Gd^{3+} and Ni^{2+} ions into BFO nanoparticles. Gd^{3+} and Ni^{2+} ions were chosen as dopants for the following two reasons. One is that they have different sizes from

*Corresponding author: Tel: +82-2-880-1458
Fax: +82-2-880-1457, e-mail: sangkoog@snu.ac.kr

those of the host ions, Bi^{3+} and Fe^{3+}, with the consequence that their doping into pure $BiFeO_3$ can cause large structural distortion of the pure $BiFeO_3$ crystal structure. The other is that the Gd^{3+} ion is magnetically active (effective magnetic moment: 7.9 μ_B) and shows a stronger magnetic interaction than do other rare-earth doped compounds [24]. Thus, the Ni^{2+} and Gd^{3+} ions play potentially important roles in the improvement of ferromagnetic coupling and in antiferromagnetic exchange coupling, respectively, even at small doping concentrations.

Meanwhile, nanostructures (especially nanoparticles) of ferroelectric perovskites show a large surface-to-volume ratio, and as such, are morphologically advantageous for obtaining surface-modified ferroelectric/magnetic properties, for example, exchange bias and long-range magnetic ordering [25, 26]. In the present work, we fabricated $(GdNi)_x(BiFe)_{1-x}O_3$ nanoparticles with x = 0, 0.025, and 0.05 by a sol-gel method, and we found a structural phase transformation according to the co-dopant concentration as well as associated enhancement in ferromagnetism along with an exchange bias effect due to modified surface spins. This work was an attempt to search for new multiferroic materials of enhanced ferromagnetism and exchange bias effect, especially for their promising technological applications to spintronics.

2. Experiments

Single-phase $(GdNi)_x(BiFe)_{1-x}O_3$ (x = 0, 0.025, 0.05) nanoparticles were synthesized using the propylene glycol-gel method. $Bi(NO_3)_3{\cdot}5H_2O$, $FeCl_3{\cdot}6H_2O$, $Gd(NO_3)_3{\cdot}6H_2O$ and $NiCl_2{\cdot}6H_2O$ solutions were mixed in stoichiometric ratios to form a precursor solution. Propylene glycol in a 1:1 mol ratio relative to metal nitrates was added and then heated at 100 °C under constant stirring until all of the liquids were evaporated from the solution. Subsequently, the final samples were calcined in ambient atmosphere at 400 °C for 2 h in order to obtain high-quality crystallization. Hereafter, the $(GdNi)_x(BiFe)_{1-x}O_3$ samples are denoted BFO, BGFNO-5, and BGFNO-10 for x = 0, 0.025, and 0.05, respectively.

The samples' crystal structure and phase purity were characterized by X-ray diffraction (XRD, D8 Advance) measurements using Cu-Kα radiation at room temperature. Rietveld refinement was performed with XRD processing software (FullProf Suit). Transmission electron microscopy (TEM) was utilized to examine the samples' morphologies (using JEOL, JEM-3000F). Raman spectrometry using λ = 514 nm line laser as excitation source was used to investigate the samples' optical phonon modes. The chemical compositions were analyzed using X-ray photoelectron spectroscopy (XPS) (Axis-HSI Instrument, Kratos Inc., USA). Temperature- and field-dependent magnetization curves were measured by the Quantum Design Physical Properties Measurement System (PPMS).

3. Results and Discussion

Figures 1(a), 1(b), and 1(c) show, for the BFO, BGFNO-5, and BGFNO-10 powder samples, respectively, the *θ-2θ* scan XRD data and their Rietveld refinements. The XRD patterns for BFO and BGFNO-5 show a rhombohedral (*R3c*) perovskite structure similar to those of pure $BiFeO_3$ samples reported in the literature [8-15]. The magnified XRD peaks at around ~32° shown in Fig. 1(d) indicate that the main peak shifts towards higher angles with increasing Gd-Ni co-doping concentration. This was due to the fact that the effective ionic radii of Gd^{3+} (0.938 Å) and Ni^{2+} (0.645 Å) are lower than those of Bi^{3+} (1.17 Å) and Fe^{3+} (0.690 Å) at the A and B sites, respectively. Moreover, for BGFNO-10, the (104) and (110) reflections peaks split and merge into a single, broad peak. These XRD patterns revealed that Gd-Ni-co-doping introduces a transformation from the rhombohedral (*R3c*) (for BFO and BGFNO-5) to the triclinic (*P1*) structure (for

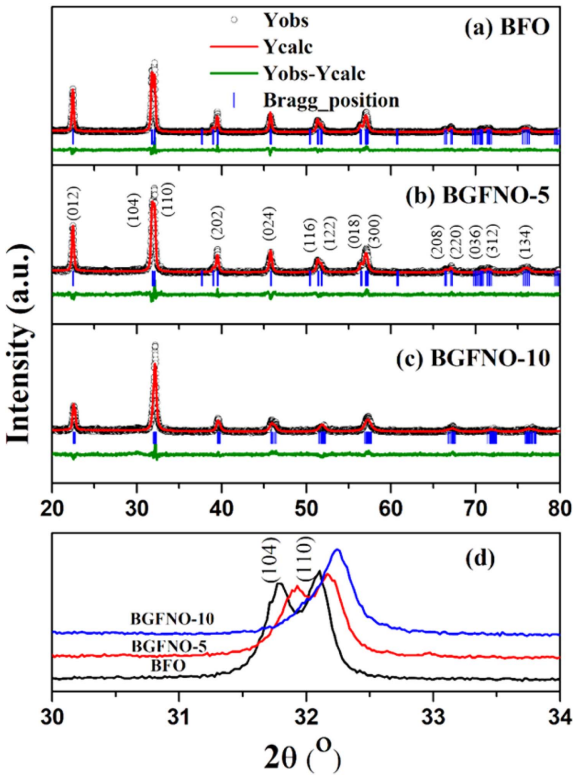

Fig. 1. (Color online) Rietveld-refined XRD patterns of (a) BFO, (b) BGFNO-5, (c) BGFNO-10 and (d) enlarged XRD patterns in 2θ range of 30-34°.

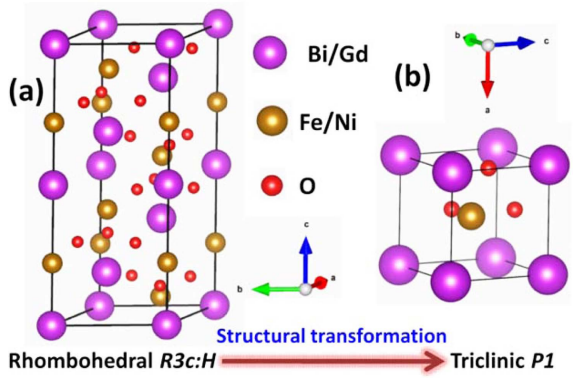

Fig. 2. (Color online) Crystal structures of (a) *R3c* and (b) *P1* space groups for pure BFO and BGFNO-10 samples, respectively.

Table 1. Crystal-structure parameters obtained from Rietveld refinements of XRD data of three different samples.

Parameters	BFO	BGFNO-5	BGFNO-10
Crystal structure	rhombohedral	rhombohedral	Triclinic
Space group	R3c	R3c	P1
a (Å)	5.5780(6)	5.5775(1)	3.9583(4)
b (Å)	5.5780(6)	5.5775(1)	3.9416(5)
c (Å)	13.8588(1)	13.8432(2)	3.9160(9)
Fe-O-Fe (°)	159.6	158.0	144.0
χ^2	1.65	1.60	1.69

BGFNO-10). A similar phenomenon has been reported by other groups [12, 27]. In the light of the present refinement results, the BFO crystal structures are schematically illustrated in Fig. 2. The Rietveld refinement parameters in Table 1 show that the angle of the Fe–O–Fe bond decreases with Gd-Ni addition in BFO.

TEM and HRTEM images of the BFO and BGFNO-10 samples are compared in Fig. 3. Figures 3(a) and 3(b) provide TEM morphology images and histogram plots of their particle-size distributions for BFO and BGFNO-10, respectively. The particle-size distribution was obtained by assuming the log-normal distribution [28] of particles having diameter (D),

$$f(D) = \frac{1}{D\sigma\sqrt{2\pi}}\exp\left\{-\frac{[\ln(D/D_P)^2]}{2\sigma^2}\right\}$$

where D_p is the median value of particle size and σ is the standard deviation. The log-normal distributions obtained from the TEM images determined the average particle size D_p of 39.6 ± 0.5 and 33.0 ± 0.70 nm for BFO and BGFNO-10, respectively. The particle-size reduction for the x = 0.05 sample can be caused by the addition of Gd and Ni ions to the $BiFeO_3$ lattices, which can inhibit the

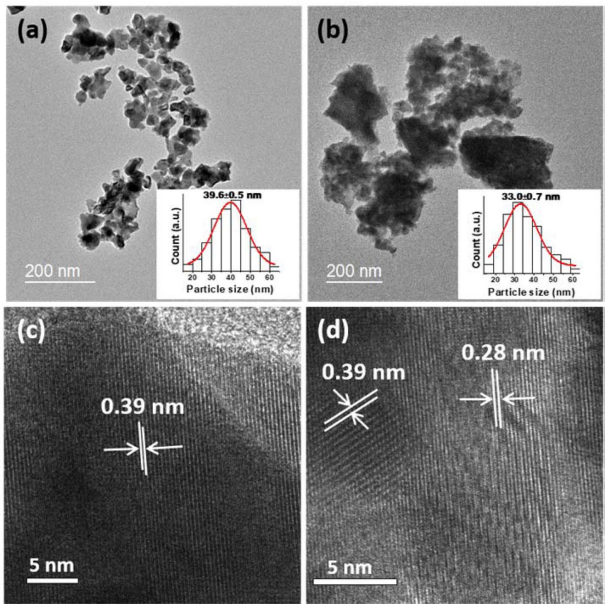

Fig. 3. (Color online) Left and right columns corresponding to pure BFO and BGFNO-10, respectively. (a), (b) show TEM images and (c), (d) show high-resolution TEM images. The insets in (a) and (b) provide histogram plots of the particle-size distributions.

growth of grains [29]. In the HRTEM images shown in Fig. 3(c), the rhombohedral *R3c* structure of BFO, as revealed by the XRD refinement, was also confirmed, by measuring the lattice distance of the (012) plane to 0.39 nm. This value is consistent with that of the rhombohedral *R3c*-structure of pure $BiFeO_3$ reported in Ref [30]. The HRTEM image of BGFNO-10 shown in Fig. 3(d) reveals inter-planar spacings of 0.39 nm and 0.28 nm along the two directions corresponding to the (100) and (101) planes, respectively, as evidenced by the crystalline triclinic (*P1*) phase and confirmed by XRD refinement. The overlapping of the lattice fringes, as shown in Fig. 3(d), can be ascribed to the agglomeration of nanoparticles of differing crystallographic orientation.

Figure 4 plots the Raman spectra of BFO, BGFNO-5 and BGFNO-10 measured at room temperature. According to a factor group analysis, the BFO has 13 Raman active modes ($\Gamma_{Raman,\ R3c}$ = 4A + 9E), indicating a highly distorted rhombohedral perovskite structure known as the *R3c* space group [12, 27, 31]. To clarify those modes, the measured spectra were fitted using their individual Lorentzian components. The fitting results are shown in Table 2. We found that three A_1-symmetry phonon and eight E-symmetry phonon modes for BFO agree well with those for BFO single crystal [32, 33] and ceramic [16]. However, BGFNO-5 showed significant broadening of the A_1-1, A_1-2, A_1-3 and E modes, as correspondent to

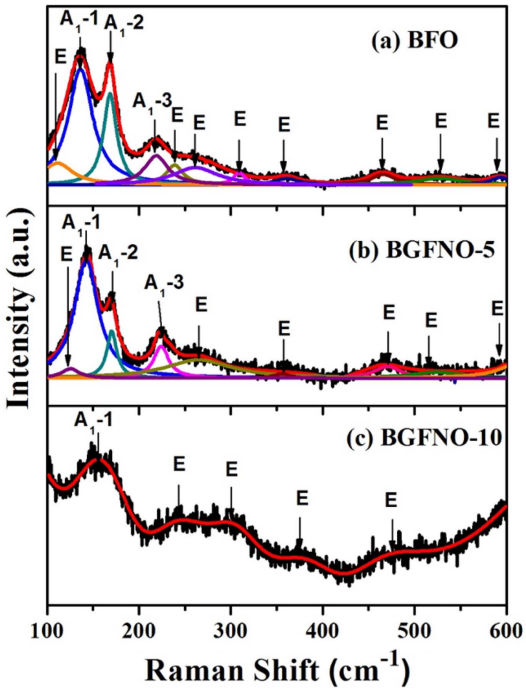

Fig. 4. (Color online) Raman spectra measured at room temperature for BFO, BGFNO-5 and BGFNO-10. The black and red lines correspond to measured and fitted spectra, respectively. The decomposed active modes are denoted by the solid lines of differing colors and arrows.

Table 2. Positions of Raman modes (cm^{-1}) for BFO, BGFNO-5 and BGFNO-10, and for $BiFeO_3$ nanocrystals reported by Fukumura *et al.* and Jaiswal *et al.*

Raman mode	Present study			Literature	
	BFO (*R3c*)	BGFNO-5 (*R3c*)	BGFNO-10 (*P1*)	Fukumura *et al.* [32]	Jaiswal *et al.* [33]
A_1-1	135	142	156	147	139
A_1-2	167	168	-	176	169
A_1-3	218	224	-	227	216
A_1-4	-	-	-	490	425
E	239	-	245	265	260
E	264	265	296	279	276
E	309	-	-	351	321
E	363	356	376	375	348
E	466	471	477	437	467
E	527	529	-	473	529
E	593	-	-	525	598
E	-	-	-	77	72
E	111	125	-	109	98

the Bi–O and Fe–O bonds [31]. It revealed that the dopant Gd and Ni had been inserted into the Bi and Fe sites of BFO, respectively. Moreover, a gradual increase in wave number was found as the doping concentration of Gd-Ni increased from x = 0 to 0.05. This mode wave number (ν) is proportional to $(k/\mu)^{1/2}$, where k is the force constant and μ is the reduced mass. As the masses of Fe^{3+} (55.84 g/mol) and Ni^{2+} (58.69 g/mol) are nearly the same and yet the Gd^{3+} (157.25 g/mol) ions are many fewer than the Bi^{3+} (208.98 g/mol) ones, a relatively lighter Gd^{3+} substitution can effect an increase in mode wave number. In the Raman scattering patterns of BGFNO-10, only five modes (A_1-1 at 156 cm^{-1}, 4E at 245, 296, 376 and 477 cm^{-1}) were detected, and the remaining A_1 and E modes nearly disappeared, implying that abrupt change of Bi-O and Fe-O covalent bonds leads to structural phase transformation [12, 31]. Thus, the gradual change of the Raman spectra and the increased areas under the curves at higher wave numbers is further suggestive of a structural transformation from *R3c* (BFO) to *P1* (BGFNO-10), similarly to the case of Nd-doped $BiFeO_3$ ceramics [27] and Pr-doped $BiFeO_3$ [12, 31]. Additionally, the broadening of the Raman peaks indicated that BGFNO-10 has a smaller particle size BFO, which also was confirmed by the TEM images.

To clarify the effects of Gd and Ni co-doping on the samples' magnetic properties, XPS measurements were carried out on BFO and BGFNO-10. The XPS survey spectra presented in Fig. 5(a) reveal the presence, in the samples, of dopant Gd and Ni as well as host Bi, Fe, and O elements. In Fig. 5(b), two main XPS peaks were observed, which corresponded to Fe $2p_{1/2}$ and Fe $2p_{3/2}$, respectively. The two split peaks at 709.6 and ~711.5 eV for the Fe $2p_{3/2}$ level verified the coexistence of Fe^{2+} and Fe^{3+} ions, respectively [34, 35] Fe^{2+} ions are unavoidable in BFO, given annealing in an air atmosphere. According to the ratio of the two peaks' areas, the concentration ratios of Fe^{3+} to Fe^{2+} ions for BFO and BGFNO-10 were

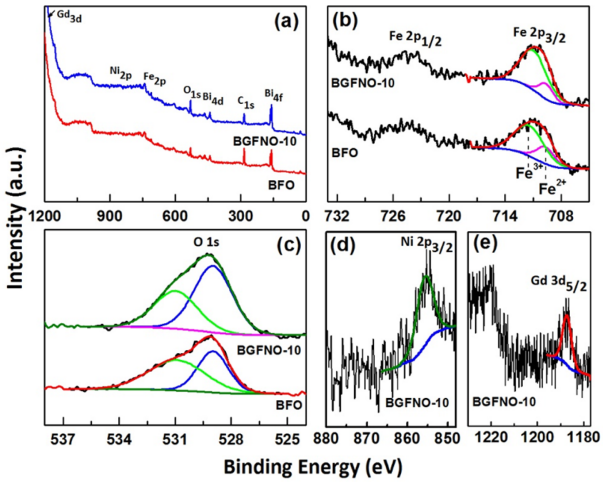

Fig. 5. (Color online) XPS spectra of both samples BFO and BGFNO-10 in binding-energy regions of (a) survey, (b) Fe 2p, (c) O 1s, (d) Ni 2p, and (e) Gd 3d peaks

estimated as 3:1 and 5:1, respectively, indicating that there were fewer Fe^{2+} ions in BGFNO-10 than in BFO. The mixed valence state of the Fe^{3+} and Fe^{2+} ions is often followed by the introduction of oxygen vacancies for maintenance of charge neutrality. Asymmetric and broad peaks appeared in the O 1s spectra, as shown in Fig. 5(c). The O 1s peaks seen at 528.9 eV and 530.9 eV corresponded to the skeletal oxygen (O_L) and oxygen vacancies (O_V), respectively [34, 36, 37]. The concentration ratios of the fitted peak areas of O_V to O_L in BFO and BGFNO-10 were 1.37 and 0.64, respectively, indicating that oxygen-vacancy concentration can be effectively reduced by Gd-Ni co-doping of pure BFO. In Fig. 5(d), the peak of the binding energy of Ni $2p_{3/2}$ at 855.3 eV represents the 2+ ionic state of Ni [38]. As shown in Fig. 5(e), meanwhile, the core-level Gd $3d_{5/2}$ binding energy found at ~1187.2 represents the oxidation state of Gd as 3+ [36, 37]. Thus, the XPS results in Figs. 5(d) and (e) manifest the substitution of Gd and Ni at the Bi and Fe sites in BFO, respectively.

Figure 6 shows magnetization hysteresis (M-H) loops measured at 300 and 5 K for BFO, BGFNO-5, and BGFNO-10 in a sweeping magnetic field up to +/-50 kOe. The observed linear slopes of the M-H loops in the higher field region indicate the existence of a predominant antiferromagnetic phase along with weak ferromagnetic ordering. The weak ferromagnetic ordering found in BFO can occur due mainly to two reasons. First, the reduction of the samples' particle size leads to a change of an antiferromagnetic-spin cycloidal structure with 62 nm wavelength in the pure $BiFeO_3$ material. The TEM image reveals a particle size of around 40 nm that breaks the $BiFeO_3$'s spin spiral structure, leading thereby to a net ferromagnetic moment. Second, observation of a net magnetic moment in an antiferromagnetic material may be caused by non-exact compensation of two magnetic sub lattices on nanoparticles' surfaces [39]. However, Gd-Ni co-doping, as compared with pure $BiFeO_3$, increases the magnetization values at both 300 and 5 K, as shown in Table 3. The M-H curves reveal that the magnetization value of 300 K at

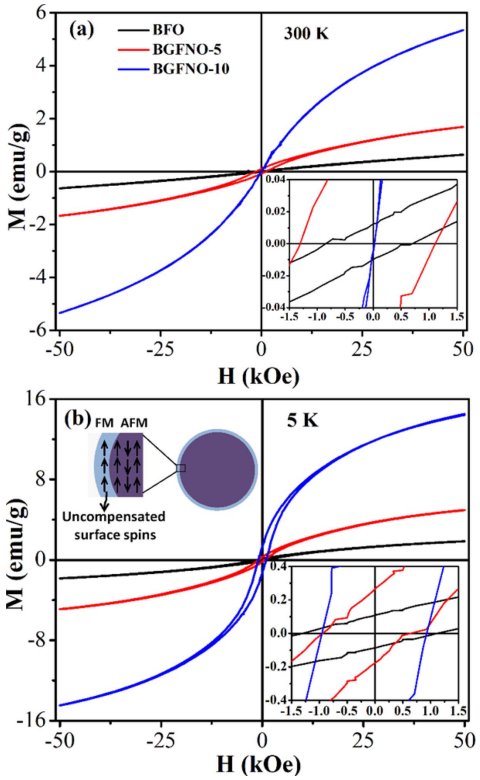

Fig. 6. (Color online) Magnetization hysteresis (M-H) loops for BFO, BGFNO-5 and BGFNO-10, as measured at (a) 300 K and (b) 5 K. The insets show magnified views of the hysteresis loops to better represent the small values of the coercivity, exchange bias field and model for the formation of nanoparticles by a shell of uncompensated spins with FM and an AFM core.

50 kOe increases from 0.62 emu/g, for BFO, to 5.32 emu/g, for BGFNO-10. The magnetization value at 300 K for BGFNO-10, 5.32 emu/g, is far larger than those obtained from (Pr, Cr) [25] and (Ho, Ni) [40] co-doped $BiFeO_3$. Enhancement of the magnetic properties of BGFNO-5 and BGFNO-10 can be accounted for in three ways. First, it can be attributed to the structural distortion resulting from the phase change of *R3c* to the *P1* structure. This phase change leads to the Fe–O–Fe bond angle's reduction

Table 3. Magnetization (M), remanent magnetization (Mr), Coercivity (Hc) and exchange bias field (H_{EB}) measured at 300 K and 5 K for BFO, BGFNO-5, and BGFNO-10.

Sample	300 K				5 K				Θ (K)
	M at 50 kOe (emu/g)	Mr (emu/g)	H_C (Oe)	H_{EB} (Oe)	M at 50 kOe (emu/g)	Mr (emu/g)	H_C (Oe)	H_{EB} (Oe)	
BFO	0.62	0.010	775	69	1.83	0.100	1214	80	55.1
BGFNO-5	1.66	0.089	1222	86	4.86	0.097	807	139	63.6
BGFNO-10	5.32	0.005	31	11	14.47	1.319	940	12	103.7

from 159.6° to 144.0° (see Table 1). Given this, the anti-symmetric Dzyaloshinskii–Moriya (DM) exchange interaction results in spin-canting of Fe^{3+} spins. The relationship between magnetization (M) and spin-canting angle (ϕ) is given as [41]

$$M = \mu_\beta g N S \sin\phi \quad (1)$$

where μ_β is the magnetic dipole moment, g is the gyromagnetic ratio, S is the magnetic spin, and N is the number of spins per unit volume. It is evident that M is directly proportional to ϕ and that the spin-canting structure's emergence is enhanced by BGFNO-5's and BGFNO-10's Gd-Ni ions. The Fe-O-Fe bond angles as calculated from the XRD Rietveld refinement were 159.6°, 158.0°, and 144.0° for BFO, BGFNO-5 and BGFNO-10, respectively. Thus, spin-canting increases due to changes in Fe-O-Fe bond angles with increasing concentrations of Gd-Ni co-dopant. Hence, the observed magnetic properties' enhancement has a strong correlation with the structural distortion that is induced by dopant substitution [42]. Second, enhancement of BGFNO-5's and BGFNO-10's magnetic properties can originate from the paramagnetic contribution of the Gd^{3+} ions' large magnetic moment (7.9 μ_B) to the net magnetization value. This can be attributed to Gd^{3+} magnetic moments' alignment in the same direction as the ferromagnetic Fe^{3+} sublattice, and in fact, Khomchenko *et al.* [43] have already reported a similar result for their Gd-Ba co-doped BFO system. Third, oxygen deficiency could increase magnetization by introduction of Fe^{2+} ions through the double exchange mechanism across Fe^{3+}–O^{2-}–Fe^{2+}, as evidenced by the existence of Fe^{2+} by XPS measurement, which mechanism is very similar to that of rare-earth-ions doping in $BiFeO_3$ [42, 43].

Moreover, the M–H loops for all of the samples manifested a shift in the negative direction, as shown in the Fig. 6 insets, indicating the existence of the exchange bias effect. The loop shift, i.e., the exchange bias field (H_{EB}) of BFO at 300 K, was about 69 Oe, which is significantly higher than the value (36 Oe) reported for bulk $BiFeO_3$ ceramic [26]. The two BGFNO samples, which had smaller particle sizes, showed H_{EB} = 86 Oe, H_{EB} = 11 Oe at 300 K for BGFNO-5 and BGFNO-10, respectively. The H_{EB} values measured at 5 K increased slightly to 80, 139, and 12 Oe for BFO, BGFNO-5, and BGFNO-10, respectively. This exchange bias effect could be interpreted in terms of exchange coupling at interfaces between ferromagnetic and antiferromagnetic regions possibly formed in small-size nanoparticles. Thus, we considered a core-shell nanoparticle model for which the ferromagnetic component arises from the nanoparticle surfaces' uncompensated spins as well as their core region's anti-ferromagnetic contribution (see upper inset in Fig. 6b) [37, 39, 44].

The temperature-dependent magnetization (M-T) curves measured under conditions of both zero fields cooling (ZFC) and field cooling (FC) at 500 Oe are plotted in Fig. 7. With increasing doping content, the magnetization values significantly increase, but the BFO data are noisy, due to the low magnetic moment at 500 Oe. In general,

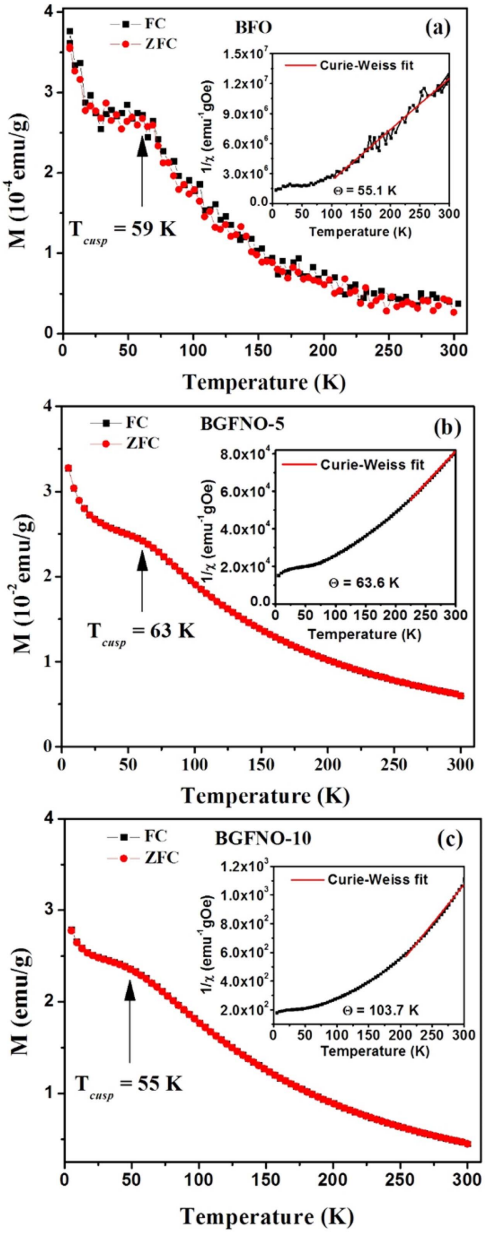

Fig. 7. (Color online) M–T curves measured under both conditions of zero fields cooling (ZFC) and fields cooling (FC) at 500 Oe: (a) BFO (b) BGFNO-5 and (c) BGFNO-10 in temperature range T = 5-300 K. The insets show the fitting of the Curie-Weiss law to the observed inverse susceptibility FC curves.

the magnetizations continuously increased with decreasing temperature, owing to the reduction of the thermal randomization of the samples' frustrated magnetic spins. None of the samples' ZFC and FC curves showed any bifurcation, as indicative of the spin-glass-like behavior [26, 45, 46]. Similar ZFC and FC curve features have been observed for Gd-Ti-co-doped BFO NPs [39]. In the present case, all of the curves showed a sharp cusp at around 59, 63 and 55 K (T_{cusp}) for BFO, BGFNO-5 and BGFNO-10, respectively, which might have been related to the magnetic domain pinning effect, as reported in Ref [47, 48]. As for the BGFNO-10, a lower T_{cusp} of about 55 K was obtained, due to possible inter-particle interaction [48]. The insets of Fig. 7 show the temperature variation of the inverse of magnetic susceptibility for the FC curves. It is clearly evident that there is a region that obeys the Curie–Weiss law as $1/\chi = (T-\Theta)/C$ [36, 37], where χ is the magnetic susceptibility, T is the absolute temperature, Θ is the Curie-Weiss temperature and C is the Curie constant. The estimated values of Θ show, with increasing Gd-Ni doping concentration, an upward trend. The values of Θ for the BFO, BGFNO-5 and BGFNO-10 samples are 55.1, 63.6 and 103.7 K, respectively. The positive value of Θ observed in the present work has also been found elsewhere [49, 50], suggesting ferromagnetic interaction in the samples. The value of Θ for our BFO sample was lower than those for *R3c*-phase $BiFeO_3$ ceramics (Θ = 90 K) reported by Gaikwad *et al.* [51] Such exchange bias effect and high magnetization values observed in Gd-Ni-co-doped $BiFeO_3$ nanoparticles can be considered to be favorable for applications in multifunctional nanodevices operating at room temperature.

4. Summary

We synthesized, using a conventional sol-gel method, Gd-Ni-co-doped $BiFeO_3$ nanoparticles of 30-40 nm average size. The rhombohedral phase with the *R3c* crystal structure for pure BFO is sustained for BGFNO-5, and subsequently is transformed to the triclinic *P1* structure for BGFNO-10. The particle size of BGFNO-10 is decreased, as confirmed by TEM measurement. XPS analysis confirms that the oxygen-vacancy concentration in BGFNO-10 is lower than that in the pure BFO nanoparticles, and also evidences that Gd^{3+} and Ni^{2+} co-doping can restrain the formation of Fe^{2+} ions. Magnetization-property enhancement is observed in Gd-Ni-co-doped $BiFeO_3$ samples relative to pure $BiFeO_3$. Such improvement could be due to the spin-canted Dzyaloshinskii–Moriya interaction manifested by the suppression of the cycloidal spin structure, since the size of the nanoparticles was less than 62 nm. At low temperature, the increase in the doped samples' spontaneous magnetizations and the positive Curie-Weiss temperature value also suggest a ferromagnetic interaction in magnetically active doped ions. The observed shift in the M-H loop could be attributed to an exchange bias effect arising between the core region of antiferromagnetic ordering and the surface region of uncompensated spins. Such moderate magnitudes of exchange bias field and coercive field make Gd-Ni-co-doped $BiFeO_3$ nanoparticles an interesting as well as attractive material for various optical and spintronic device applications at room temperature.

Acknowledgements

This research was supported by the Basic Science Research Program through the National Research Foundation of Korea (NRF) funded by the Ministry of Science, ICT & Future Planning (NRF-2018R1A2A1A05078913). We are also thankful to the Institute of Engineering Research at Seoul National University for providing some facilities.

References

[1] S.-W. Cheong and M. Mostovoy, Nat. Mater. **6**, 13 (2007).
[2] T. Kimura, T. Goto, H. Shintani, K. Ishizaka, T. Arima, and Y. Tokura, Nature **426**, 55 (2003).
[3] D. T. Huong Giang, P. A. Duc, N. T. Ngoc, N. T. Hien, and N. H. Duc, J. Magn. **17**, 308 (2012).
[4] D. Bilican, E. Menendez, J. Zhang, P. Solsona, J. Fornell, E. Pellicer, and J. Sort, RSC Adv. **7**, 32133 (2017).
[5] D. Lebeugle, D. Colson, A. Forget, M. Viret, P. Bonville, J. F. Marucco, and S. Fusil, Phys. Rev. B: Condens. Matter Mater. Phys. **76**, 024116 (2007).
[6] M. Roy, S. Jangid, S. K. Barbar, and P. Dave, J. Magn. **14**, 62 (2009).
[7] Je-Geun Park, M. D. Le, J. Jeong, and S. Lee, J. Phys.: Condens. Matter **26**, 433202 (2014).
[8] I. Levin, M. G. Tucker, H. Wu, V. Provenzano, C. L. Dennis, S. Karimi, T. Comyn, T. Stevenson, R. I. Smith, and I. M. Reaney, Chem. Mater. **23**, 2166 (2011).
[9] N. Jeon, D. Rout, I. W. Kim, and S.-J. L. Kang, Appl. Phys. Lett. **98**, 072901 (2011).
[10] D. Chen *et al.*, Nano Lett. **17**, 5823 (2017).
[11] J. Schiemer, R. L. Withers, M. A. Carpenter, Y. Liu, J. L. Wang, L. Noren, Q. Li, and W. Hutchison, J. Phys.: Condens. Matter **24**, 125901 (2012).
[12] S. K. Srivastav, N. S. Gajbhiye, and A. Banerjee, J. Appl. Phys. **113**, 203917 (2013).
[13] Q. Y. Xu, H. F. Zai, D. Wu, T. Qiu, and M. X. Xu, Appl. Phys. Lett. **95**, 112510 (2009).
[14] A. A. Belik, A. M. Abakumov, A. A. Tsirlin, J. Hader-

mann, J. Kim, G. V. Tendeloo, and E. Takayama-Muromachi, Chem. Mater. **23**, 4505 (2011).
[15] X. Tang, J. Dai, X. Zhu, and Y. Sun, J. Alloys Compd. **552**, 186 (2013).
[16] L. Hongri and S. Yuxia, J. Phys. D: Appl. Phys. **40**, 7530 (2007).
[17] P. Suresh, P. D. Babu, and S. Srinath, J. Appl. Phys. **115**, 17D905 (2014).
[18] S. Chaturvedi, R. Bag, V. Sathe, S. Kulkarni, and S. Singh, J. Mater. Chem. C, **4**, 780 (2016).
[19] V. A. Khomchenko, D. V. Karpinsky, A. L. Kholkin, N. A. Sobolev, and G. N. Kakazei, J. Appl. Phys. **108**, 074109 (2010).
[20] F. X. Yan, G. Y. Zhao, N. Song, N. Zhao, and Y. Q. Chen, J. Alloys Comp. **570**, 19 (2013).
[21] P. Kumar, N. Shankhwar, A. Srinivasan, and M. Kar, J. Appl. Phys. **117**, 194103 (2015).
[22] K. G. Yang, Y. L. Zhang, S. H. Yang, and B. Wang, J. Appl. Phys. **107**, 124109 (2010).
[23] W. W. Mao, X. F. Wang, Y. M. Han, X. A. Li, Y. T. Li, Y. F. Wang, Y. W. Ma, X. M. Feng, T. Yang, J. P. Yang, and W. Huang, J. Alloys Comp. **584**, 520 (2014).
[24] W. Hu, Y. Chen, H. Yuan, G. Li, Y. Qiao, Y. Qin, and S. Feng, J. Phys. Chem. C **115**, 8869 (2011).
[25] R. Das, G. G. Khan, S. Varma, G. D. Mukherjee, and K. Mandal, J. Phys. Chem. C **117**, 20209 (2013).
[26] D. S. Rana, D. G. Kuberkar, and S. K. Malik, Phys. Rev. B **73**, 064407 (2006).
[27] A. Kumar and D. Varshney, Ceram. Inter. **38**, 3935 (2012).
[28] S. K. S. Patel, K. Dewangan, S. K. Srivastav, and N. S. Gajbhiye, Current App. Phys. **14**, 905 (2014).
[29] S. K. S. Patel, S. Kurian, and N. S. Gajbhiye, Mater. Res. Bull. **48**, 655 (2013).
[30] S. Mohan and B. Subramanian, RSC Adv. **3**, 23737 (2013).
[31] M. Muneeswaran, R. Dhanalakshmi, and N. V. Giridharan, Ceram. Inter. **41**, 8511 (2015).
[32] H. Fukumura, H. Harima, K. Kisoda, M. Tamada, Y. Noguchi, and M. Miyayama, J. Magn. Magn. Mater. **310**, 367 (2007).
[33] A. Jaiswal, R. Das, K. Vivekanand, P. M. Abraham, S. Adyanthaya, and P. Poddar, J. Phys. Chem. C **114**, 2108 (2010).
[34] P. W. Ye, G. Tan, X. Yan, H. Ren, and A. Xia, RSC Adv. **5**, 43594 (2015).
[35] S. Thampy, N. Ashburn, T. J. Martin, C. Li, Y. Zheng, J. Y. Chan, K. Cho, and Julia W. P. Hsu, RSC Adv. **8**, 28 (2018).
[36] S. K. S. Patel, P. Dhak, M-K. Kim, J-H. Lee, M. Kim, and S-K. Kim, J. Magn. Magn. Mater. **403**, 155 (2016).
[37] S. K. S. Patel, J-H. Lee, M-K. Kim, B. Bhoi, and S-K. Kim, J. Mater. Chem. C **6**, 526 (2018).
[38] G. Wang, Y. Ling, X. Lu, T. Zhai, F. Qian, Y. Tong, and Y. Li, Nanoscale **5**, 4129 (2013).
[39] M. A. Basith, F. A. Khan, B. Ahmmad, S. Kubota, F. Hirose, D.-T. Ngo, Q.-H. Tran, and K. Mølhave, J. Appl. Phys. **118**, 023901 (2015).
[40] J. S. Park, Y. J. Yoo, J. S. Hwang, J.-H. Kang, B. W. Lee, and Y. P. Lee, J. Appl. Phys. **115**, 013904 (2014).
[41] S. Bharathkumar, M. Sakar, K. R. Vinod, and S. Balakumar, Phys. Chem. Chem. Phys. **17**, 17745 (2015).
[42] N. H. Hong, N. T. Huong, Tae-Young Kim, S. Goumri-Said, and M. B. Kanoun, J. Phys. Chem. C **119**, 14351 (2015).
[43] V. A. Khomchenko, V. V. Shvartsman, P. Borisov, W. Kleemann, D. A. Kiselev, I. K. Bdikin, J. M. Vieira, and A. L. Kholkin, J. Phys. D: Appl. Phys. **42**, 045418 (2009).
[44] H. Ahmadvand, H. Salamati, P. Kameli, A. Poddar, M. Acet, and K. Zakeri, J. Phys. D: Appl. Phys. **43**, 245002 (2010).
[45] L. Fang, J. Liu, S. Ju, F. Zheng, W. Dong, and M. Shen, Appl. Phys. Lett. **97**, 242501 (2010).
[46] K. Parekh and R. V. Upadhyay, Journal of Nanofluids **1**, 93 (2012).
[47] C. R. Sankar and P. A. Joy, Phys. Rev. B **72**, 024405 (2005).
[48] F. Huang, Z. Wang, X. Lu, J. Zhang, K. Min, W. Lin, R. Ti, T. T. Xu, J. He, C. Yue, and J. Zhu, Sci. Rep. **3**, 2907 (2013).
[49] X. Ma, Sheng-Min Hu, Chun-Hong Tan, Yong-Fan Zhang, Xu-Dong Zhang, Tian-Lu Sheng, and Xin-Tao Wu, Inorg. Chem. **52**, 11343 (2013).
[50] Xin-Yi Wang, M. G. Hilfiger, A. Prosvirin, and K. R. Dunbar, Chem. Commun. **46**, 4484 (2010).
[51] V. M. Gaikwad and S. A. Acharya, J. Appl. Phys. **114**, 193901 (2013).